

# Surface acoustic wave-assisted spin-orbit torque switching of the Pt/Co/Ta heterostructure

Cite as: Appl. Phys. Lett. **119**, 012401 (2021); doi: [10.1063/5.0055261](https://doi.org/10.1063/5.0055261)

Submitted: 27 April 2021 · Accepted: 16 June 2021 ·

Published Online: 6 July 2021



View Online



Export Citation



CrossMark

Y. Cao,<sup>1</sup> X. N. Bian,<sup>2</sup> Z. Yan,<sup>1</sup> L. Xi,<sup>1</sup> N. Lei,<sup>2</sup> L. Qiao,<sup>1</sup> M. S. Si,<sup>1</sup> J. W. Cao,<sup>1</sup> D. Z. Yang,<sup>1,a)</sup> and D. S. Xue<sup>1,a)</sup>

## AFFILIATIONS

<sup>1</sup>Key Laboratory for Magnetism and Magnetic Materials of Ministry of Education, Lanzhou University, Lanzhou 730000, China

<sup>2</sup>Fert Beijing Institute, MIIT Key Laboratory of Spintronics, School of Integrated Circuit Science and Engineering, Beihang University, Beijing 100191, China

<sup>a)</sup>Authors to whom correspondence should be addressed: [yangdzh@lzu.edu.cn](mailto:yangdzh@lzu.edu.cn) and [xueds@lzu.edu.cn](mailto:xueds@lzu.edu.cn)

## ABSTRACT

Current-induced spin-orbit torque (SOT) allows for highly efficient control of magnetization for the magnetic memory and the logic application, but its high critical current density  $J_c$  limits its applications. Here, we report that the surface acoustic wave (SAW) presents a promising approach for reducing  $J_c$  in Pt/Co/Ta heterostructures with perpendicular anisotropy. By the second harmonic Hall measurements, we find that the damping-like SOT effective field is almost the same with or without SAW, implying that the reduction of  $J_c$  does not originate from the enhancement of the SOT. However, the current-induced domain wall velocity  $v$  under SAW is greatly enhanced. By fitting with the creep law under SAW, we find that  $\ln v$  is linear with SAW power ( $P$ ), which reveals that the effective pinning barrier is reduced linearly with increasing  $P$ . This feature can be well described by the time average of the periodically accumulated nucleation probability under SAW. The results shed light on the application of SAW-assisted SOT devices for low consumption storage.

Published under an exclusive license by AIP Publishing. <https://doi.org/10.1063/5.0055261>

Spin-orbit torques (SOTs) in ferromagnetic metal (FM)/heavy metal (HM) heterostructures induced by the in-plane charge current have attracted great research interest.<sup>1,2</sup> Due to both the Rashba effect at the FM/HM interface and the spin Hall effect in the bulk of HM, the applied in-plane charge current can be converted to the spin current, which exerts SOTs on the magnetization of the FM layer.<sup>3–5</sup> So far, SOT has been demonstrated as an efficient approach to switch the magnetization, drive chirality-dependent domain wall (DW) motion, and excite high-frequency magnetization oscillations.<sup>6</sup> However, its high critical current density ( $J_c$ ) still limits its applications.

In order to reduce  $J_c$ , one promising route is to use the surface acoustic wave (SAW),<sup>7</sup> which is an elastic wave with a specific frequency (typically 0.1–1 GHz) propagating on the surface of piezoelectric materials. Owing to its wave property, SAW allows one to nonlocally switch the magnetic bits, which makes the SAW device of simple structure, flexible design, and easy integration. More importantly, unlike the time-independent stress,<sup>8,9</sup> SAW with a time-varying strain could realize precessional magnetization switching, which can effectively reduce the reversal fields.<sup>10–12</sup> For resonant precession, SAW can directly induce the acoustic ferromagnetic resonance or spin-wave resonance.<sup>13,14</sup> Even for non-resonance precession, SAW can also significantly reduce the coercivity of the ferromagnet.<sup>15–18</sup>

This is because that the domain nucleation barrier is significantly reduced by SAW. Very recently, owing to the spin-rotation coupling effect,<sup>19,20</sup> SAW has been proposed to generate the spin currents in the nonmagnetic metals, which provides another attractive method for SAW-assisted SOT switching. In contrast to the spin-rotation coupling effect where the spin angular momentum is converted from the mechanical angular momentum, for the acoustic spin Hall effect,<sup>21</sup> an a.c. spin current is directly generated from the lattice motion driven by SAW and interacts with the ferromagnet layer due to spin-transfer torque. As a result, a net d.c. backflow spin current is profiled in heavy metal, which induced the Hall voltage due to the inverse spin Hall effect. In contrast to the spin-rotation coupling effect existing in light metals, the acoustic spin Hall effect exists in heavy metals. So far, the previous works mainly focus on the SAW-assisted magnetic field switching; however, the SAW-assisted SOT switching has not been carried out yet.

In this work, we report that SAW presents a promising approach not only for reducing  $J_c$ , but also for enlarging the DW velocity  $v$  in Pt/Co/Ta heterostructures with perpendicular anisotropy. With the assistance of SAW,  $J_c$  is reduced from  $2.9 \times 10^6$  to  $2.4 \times 10^6$  A cm<sup>-2</sup>, and  $v$  increases two times up to 140 mm/s. We find that the current ( $J$ ) driven DW motion under different SAW power ( $P$ ) can be described by  $\ln v = C_0 - C_P P - C_J J^{-1/4}$ , where  $C_0$ ,  $C_P$ , and  $C_J$  are constant

coefficients. Through analyzing the SOT-driven DW creep law and the combination of the modified droplet DW model, we further reveal that the reduction of  $J_c$  under SAW is caused by the periodical accumulation of nucleation probability under SAW.

Figure 1(a) shows the schematic of the SAW device configuration and the SOT device structure. SAW is launched and detected by two sets of Ta (5)/Al (70 nm) interdigital transducers (IDTs). The distance between the two IDTs is  $L = 7.2$  mm. The IDTs were patterned on 128° Y-cut LiNbO<sub>3</sub> by liftoff technology. Each IDT consists of 50 finger pairs, where the acoustic aperture  $W = 1800$   $\mu\text{m}$ . The finger width and spacing are both designed 12, resulting in the SAW wavelength  $\lambda = 48$   $\mu\text{m}$ . The propagation direction of SAW is along the  $x$ -axis, which is perpendicular to the in-plane crystallographic  $X$ -direction of LiNbO<sub>3</sub>, i.e., the (1 0 0) direction of the hexagonal system.<sup>22</sup> The typical SOT device with stacks of Ta(3)/Pt(3)/Co(0.7)/Ta(4)/AlO<sub>x</sub>(1) (thickness in nm) with perpendicular anisotropy was deposited between the two IDTs. Since Ta and Pt have opposite spin Hall angles, the SOTs with Pt/Co/Ta structure are greatly enhanced.<sup>23</sup> The base pressure of magnetron sputtering was below  $5.0 \times 10^{-5}$  Pa. Then, the film was patterned to a 10  $\mu\text{m}$  wide Hall bar by lithography technology to study SOT switching.

Figure 1(b) shows the SAW time-domain measurement results, where the input rf frequency  $f = 76.0$  MHz is the fundamental frequency of SAW ( $f_0$ ). We used Agilent 81150A signal generator to generate a series of pulsed rf signals via “triggered burst” mode. The burst contains 40-period sinewaves, which are set to a frequency of  $f_0$  to excite the SAW. The burst repetition is generated by using the internal trigger source of Agilent 81150A with a frequency of 100 kHz. To observe the SAW signal in the oscilloscope, the internal trigger source of Agilent 81150A is also used as the output trigger to synchronize the oscilloscope. Considering the group velocity difference between the electromagnetic wave and SAW, the delayed response signal with a delay time  $t_d = 2.07$   $\mu\text{s}$  is attributed to the SAW. The SAW velocity

$v_{\text{SAW}}$  can be calculated by  $v_{\text{SAW}} = \frac{L}{t_d} = 3480$  m/s, which is consistent with the equation  $v_{\text{SAW}} = f_0 \lambda$ . Figure 1(c) shows the reflection ( $S_{11}$ ) and transmission ( $S_{21}$ ) spectra of SAW, measured by a vector network analyzer. We observe a sharp peak in  $S_{21}$  at  $f_0$ , indicating that the rf powers can be efficiently transmitted via SAW. According to  $S_{11}$ , we can obtain the acoustic power  $P_a = \frac{1}{2} k^2 \Delta |S_{11}|^2 P$ ,<sup>14</sup> where  $P$  is the input power of SAW and  $k^2 = 5\%$  is the electromechanical coupling coefficient of LiNbO<sub>3</sub>. For  $P = 232$ ,  $P_a = 2.5$  mW, which results in a longitudinal strain  $\epsilon_{xx} = 1.1 \times 10^{-5}$  according to  $\epsilon_{xx} = \frac{2\pi}{\lambda} u_x = \frac{2\pi}{\lambda} * 0.6 \sqrt{\frac{P_a}{2\pi M f_0 W}}$  where  $u_x$  is the longitudinal displacement and  $M = 1.4 \times 10^{11}$  J/m<sup>3</sup> is a material constant related to the elastic constant of LiNbO<sub>3</sub>.<sup>24</sup> For Rayleigh SAW,  $\epsilon_{xx}$  is the main strain component, and it induces the magnetoelastic energy  $F_{ME} = B_3 \epsilon_{xx}(t)(1 - m_z^2)$ ,<sup>25</sup> where  $B_3 = 2.8 \times 10^7$  J/m<sup>3</sup> is the magnetoelastic coupling coefficient for hcp Co, and the main magnetization component  $m_z$  is considered.

Figures 2(a) and 2(b) show the SOT switching of Pt/Co/Ta structure under SAW at resonance and off resonance, respectively. The sharp switching of anomalous Hall resistance ( $R_H$ ) induced by current density  $J$  indicates a good perpendicular anisotropy of the Co layer. We observe a significant reduction of  $J_c$  under SAW at resonance with increasing  $P$ ; however, a tiny reduction of  $J_c$  is observed at off resonance. For the various  $f$  of SAW,  $J_c$  all reduces linearly with increasing  $P$ , as shown in Fig. 2(c). More importantly, the reduction of  $J_c$  gradually increases when  $f$  approaches  $f_0$  and becomes the maximum at  $f_0$ .

The  $f$  dependence of the reduction slope  $k_f = \left| \frac{\partial J_c(P)}{\partial P} \right|$  is shown in Fig. 2(d), which is exactly similar to the  $S_{21}$  curve in Fig. 1(c). This similarity confirms that the reduction of  $J_c$  is caused by SAW, not the microwave<sup>26–28</sup> or heat effect.<sup>29</sup>

Next, we will further quantitatively measure the SOT-induced damping-like effective field ( $H_{DL}$ ) under SAW by using the harmonic

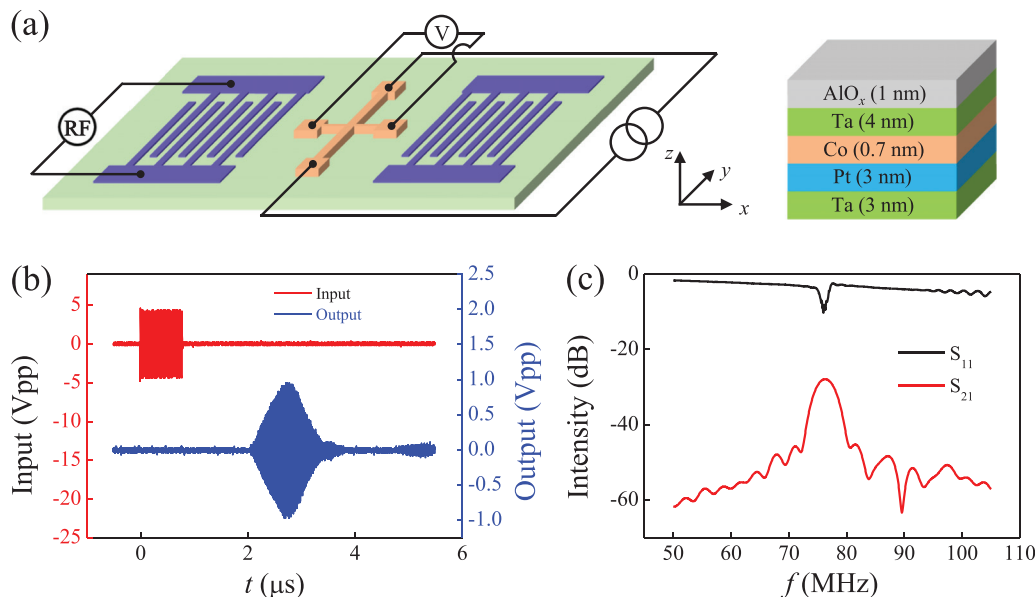
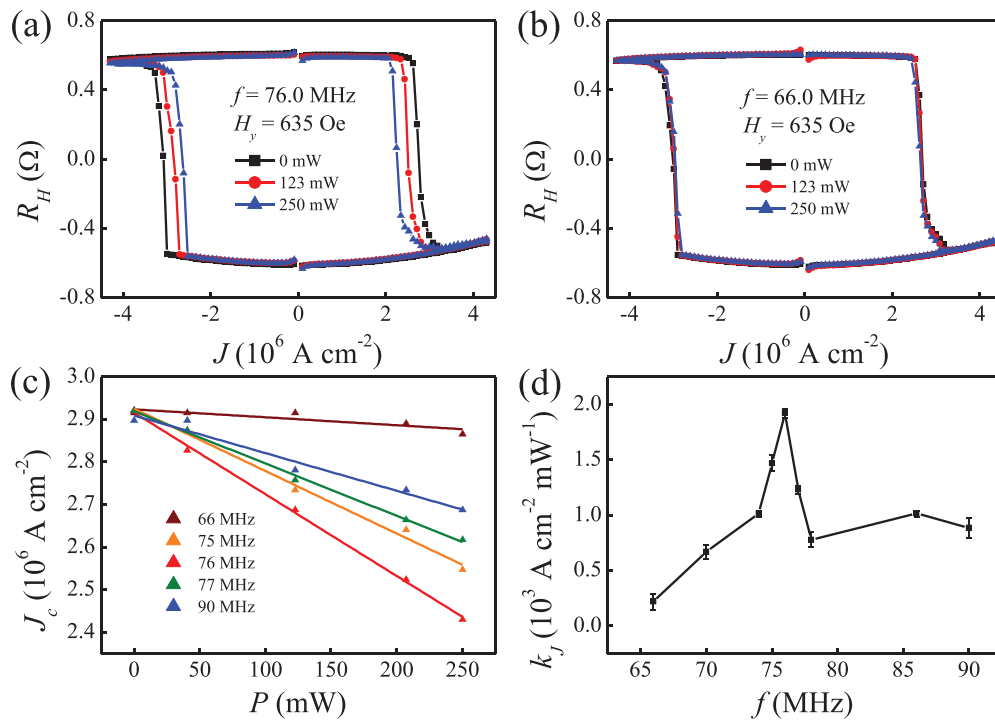


FIG. 1. (a) Schematic of the SAW device configuration and SOT device structure. (b) The time-domain measurement results of the SAW device. The input signal (red line) was applied on one side IDT; the response signal (blue line) was detected on the other side IDT. (c) The reflection ( $S_{11}$ ) and transmission ( $S_{21}$ ) spectra of SAW.



**FIG. 2.** The SOT switching under SAW (a) at resonance and (b) off resonance, respectively, where an external magnetic field  $H_y = 635$  Oe is applied to break the inversion symmetry. (c) The  $P$  dependence of  $J_c$  under SAW with different  $f$ . The symbols are the data points. The solid lines represent the linear fitting of the data. (d) The  $f$  dependence of the slope  $k_j$ . The error bars represent fitting errors.

Hall measurements.<sup>30,31</sup> An in-plane a.c. current ( $I = I_0 \sin \omega t_a$ ) with  $I_0 = 3$  mA, and  $\omega = 133$  Hz is applied through the heavy metal (Pt and Ta) to generate the SOTs, which induces a small oscillation of Co magnetization away from its equilibrium direction. Such oscillations will generate the second harmonic Hall voltages  $V_{2\omega}$ . To obtain  $H_{DL}$ , we measured the first ( $V_{1\omega}$ ) and the second ( $V_{2\omega}$ ) harmonic Hall voltages as the function of  $H_y$ .  $V_{1\omega}$  under SAW in Figs. 3(a) and 3(b) both have similar parabolic behaviors for the magnetization along  $+z$  and  $-z$ , respectively. The almost same quadratic coefficients indicate that the magnetization is mainly changed by  $H_y$ , not the SAW. However, there is an obvious shift of  $V_{1\omega}$  curve under SAW with different powers, which may arise from the magneto-acoustic effect.<sup>32</sup> Similar to previous SOT results,  $V_{2\omega}$  under SAW in Fig. 3(c) is still linear with  $H_y$ . Thus, we can obtain  $H_{DL}$  under SAW using the formula  $H_{DL} = -2 \frac{\partial V_{2\omega}}{\partial H_y} / \frac{\partial^2 V_{1\omega}}{\partial H_y^2}$ .<sup>30</sup> We found that  $H_{DL}$  is almost the same under SAW in Fig. 3(d). This indicates that the reduction of  $J_c$  under SAW is not caused by the enhancement of SOT. Besides,  $H_{DL}$  for  $+M_z$  and  $-M_z$  is asymmetric. We think the asymmetry of  $H_{DL}$  in our system may come from the system symmetry breaking, such as the anisotropy developed during the film deposition process,<sup>33</sup> the formation of multiple domains, or the preexisting non-reversed domains acting as a pinning field.<sup>34</sup>

In order to understand the mechanism of the reduction of  $J_c$  under SAW, we further observed the current-induced DW motion using a polar magneto-optical Kerr microscope. Owing to the damping-like SOT acting on the chiral Néel-type DW, an out-of-plane effective magnetic field replaces the external magnetic field to drive

DW motion. In our case, the current pulse width is 0.1 ms, and the current pulse interval is 2 s to avoid the accumulation of Joule heat. As shown in Fig. 4(a), DW without and with SAW both have the obvious tilting effects, which are induced by the Dzyaloshinskii–Moriya interaction (DMI).<sup>35</sup> When the current passed through the Hall bar, the current-induced SOT leads to a rotation of the DW magnetization away from the Néel configuration. This will increase the energy of DMI since DMI energetically favors the Néel configuration. As a result, the DW tilts by an angle to balance the competition between the SOT effect and DMI effect, despite inducing a higher DW energy due to the larger DW surface. Notably, after one pulse, the movement of DW with SAW is longer than that of DW without SAW. In order to accurately calculate the DW velocity  $v$ , we subtract the magnetic domain images at two moments  $t_1$  and  $t_2$  with the software Image J.<sup>36</sup> Then the area of the DW movement by image subtract can be directly obtained by Image J. The DW velocity  $v$  is calculated by dividing the area of the DW movement by the width of the Hall bar ( $10 \mu\text{m}$ ) and the time ( $t_{DW} = t_2 - t_1$ ). It should be noted the domain velocity is measured 5 times and averaged. As shown in Fig. 4(b), the DW velocity  $v$  increases significantly with  $P$  at resonance; however, no  $v$  enhancement is observed when  $f$  is far away from  $f_0$ , which gives an identical trend with the  $f$  dependence of the reduction of  $J_c$ . At resonance, the DW velocity  $v$  increases exponentially as a function of  $J$ , as shown in Fig. 4(c). Moreover,  $v$  increases more sharply as  $P$  increases.

It has been reported that the magnetic DW motion driven by low current density follows the creep regime,<sup>37</sup> where the DW velocity is

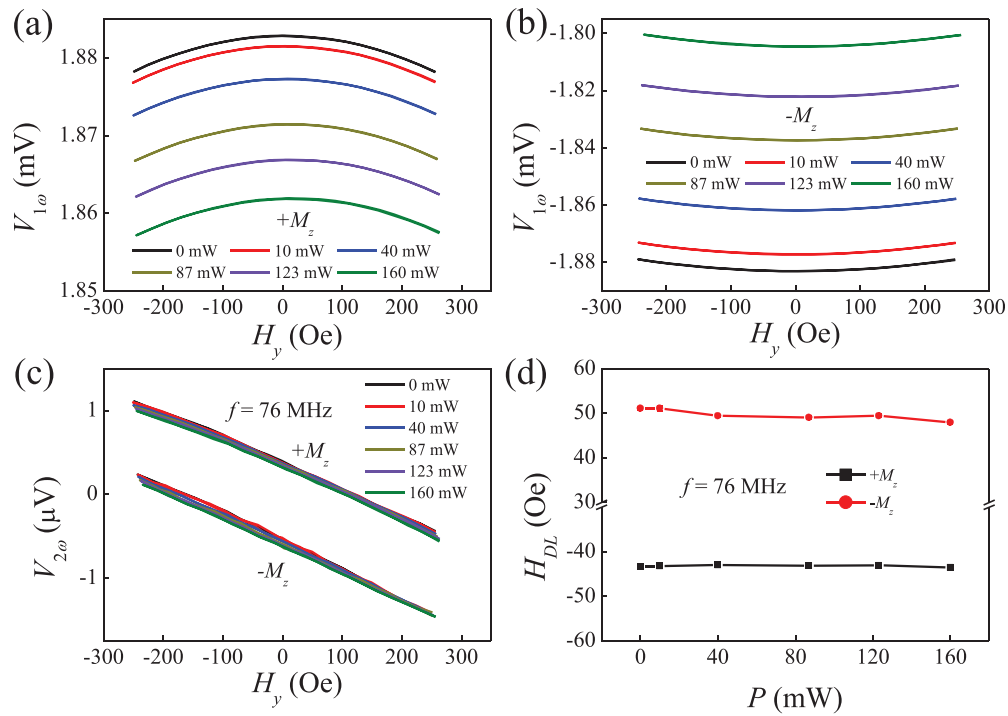


FIG. 3.  $V_{1\omega}$  as a function of  $H_y$  for magnetization along (a)  $+z$  axis and (b)  $-z$  axis under SAW with different  $P$ , respectively. (c)  $V_{2\omega}$  as a function of  $H_y$  under SAW with different  $P$ . (d)  $H_{DL}$  as a function of  $P$  under SAW.

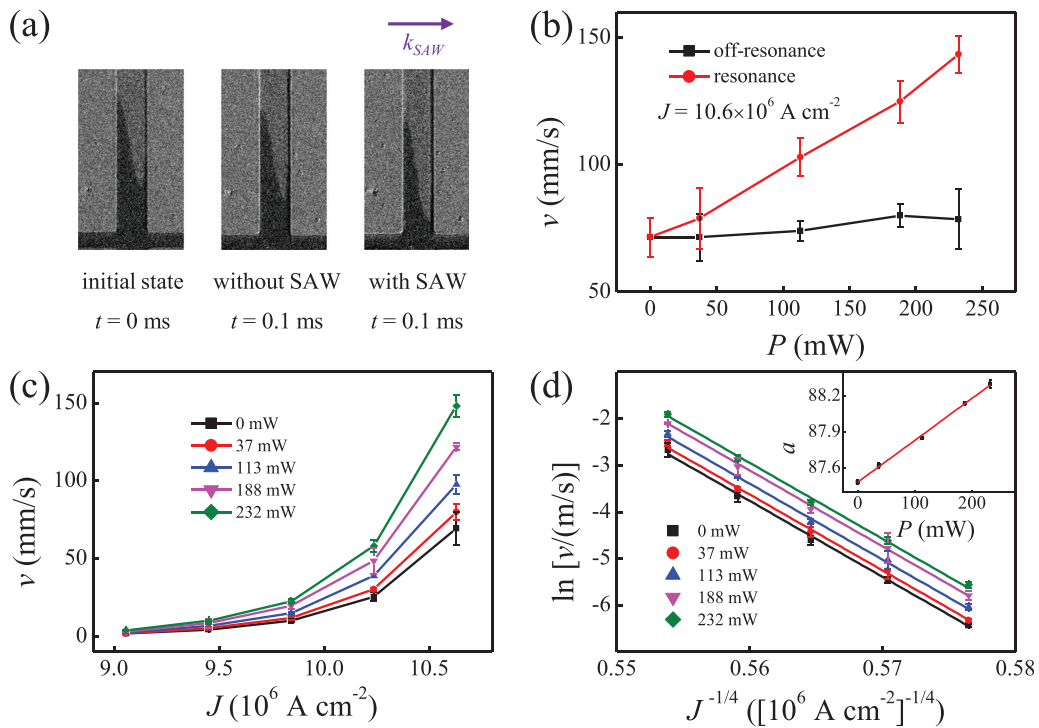


FIG. 4. (a) The SOT-induced DW motion images without and with SAW after one pulse. (b) The  $P$  dependence of the DW velocity  $v$  under SAW at resonance and off resonance. (c) The  $J$  dependence of  $v$  under SAW with different  $P$ . (d) The  $J^{-1/4}$  dependence of  $\ln v$  under SAW with different  $P$ . The solid lines correspond to the linear fit. Inset: The fitting intercept  $a$  as a function of  $P$ . The solid line represents the linear fit.

described by  $v = v_0 \exp\left(-\frac{\Delta E(J,P)}{k_B T}\right)$ , where  $v_0$  is the characteristic velocity,  $k_B$  is the Boltzmann constant,  $T$  is the temperature, and  $\Delta E(J, P)$  is an effective pinning energy barrier. In our case,  $\Delta E(J, P)$  is not only related to the  $J$ , but also influenced by SAW with different power  $P$ . Considering the perturbation expansion of SAW, we can obtain  $\Delta E(J, P) = \Delta E(J, 0) + \frac{\partial \Delta E}{\partial P} P$ , where  $\Delta E(J, 0)$  is the depinning energy without SAW, and  $\frac{\partial \Delta E}{\partial P}$  is the first-order approximation of SAW-induced  $\Delta E$ . Since  $\Delta E(J, 0) = U_c \left(\frac{J}{J_d}\right)^{-1}$ ,<sup>37</sup> where  $U_c$  is the characteristic pinning energy scale and  $J_d$  is the depinning current, we can obtain the SAW modified creep law as follows:

$$\ln v = \ln v_0 - \frac{1}{k_B T} \frac{\partial \Delta E}{\partial P} P - \frac{U_c}{k_B T} J_d^{-1} J^{-1}. \quad (1)$$

The linear behavior of  $\ln v$  as a function of  $J^{-1}$  in Fig. 4(d) verifies that DW motions under SAW are still in the creep regime. For  $P = 0$  mW, we can obtain  $\frac{U_c}{k_B T} J_d^{-1} = 163 (10^6 \text{ A cm}^{-2})^{-1}$  by linear fitting. As  $P$  increases in Fig. 4(d), the slope is almost the same, but the intercept  $a$  gradually increases. This indicates that  $\frac{\partial \Delta E}{\partial P}$  in Eq. (1) is independent of  $J$ , and  $a = \ln v_0 - \frac{1}{k_B T} \frac{\partial \Delta E}{\partial P} P$  only depends on  $P$ . In the inset of Fig. 4(d), we further find that  $a$  is almost linear with  $P$ , indicating  $\frac{1}{k_B T} \frac{\partial \Delta E}{\partial P} = -3.5 \times 10^{-3} \text{ mW}^{-1}$  is a constant. Therefore, according to our fitting results, the SAW modified creep law can be further simplified as

$$\ln v = C_0 - C_P P - C_J J^{-1}, \quad (2)$$

where  $C_0$ ,  $C_P$ , and  $C_J$  are constant coefficients. The fitting results also reveal that the effective pinning energy barrier  $\Delta E$  decreases linearly with SAW input power  $P$ , which results in the increase of DW velocity. The enhancement of DW velocity may also derive from the acoustic spin Hall effect,<sup>21</sup> which requires further study.

The observed linear lowering of  $\Delta E$  with  $P$  can be explained by the lowering of the strain-dependent domain nucleation energy under SAW. According to the droplet model,<sup>16</sup> when the nucleation of a cylindrical domain is formed, the total energy barrier  $\Delta E_{tot} = \frac{\pi d \sigma^2}{2\mu_0 H M_s}$ , where  $\sigma$  is the DW energy per unit area,  $d$  is the layer thickness, and  $H$  is the external magnetic field or SOT-induced effective magnetic field. Due to the magnetoelastic energy  $F_{ME}$ , the DW energy  $\sigma$  is given by  $4\sqrt{A_{ex}(K_u + B_3 \varepsilon_{xx}(t))}$ , where  $A_{ex} = 4.0 \times 10^{-11} \text{ J/m}$  is the exchange stiffness and  $K_u = 3.5 \times 10^5 \text{ J/m}^3$  is the perpendicular anisotropy. Since  $\sigma$  under SAW is time-dependent,  $\Delta E_{tot}$  is time-varying, as shown in Fig. 5(a). Here we assume a localized lowering of the DW energy  $\sigma^* = \gamma \sigma$  due to defects or magnetic anisotropy inhomogeneities, and  $\gamma = 9.0 \times 10^{-2}$  in order to match our experimental data.

Since the SAW is propagating and not stationary, the domain nucleation probability during a magnetic field duration time  $T_f$  is gradually accumulated as follows:<sup>16</sup>

$$\ln(1 - P_{nuc}(T_f, H)) = -\frac{1}{\tau_0} \int_0^{T_f} \exp\left(-\frac{\Delta E_{tot}(t, H)}{k_B T}\right) dt, \quad (3)$$

where the relaxation time  $\tau_0 = 10$  ps. When  $\varepsilon_{xx} = 1.1 \times 10^{-5}$  at  $P = 232$  mW, the calculation result of  $\ln(1 - P_{nuc})$  [Fig. 5(b)] decreases faster than that without SAW, indicating that the domain

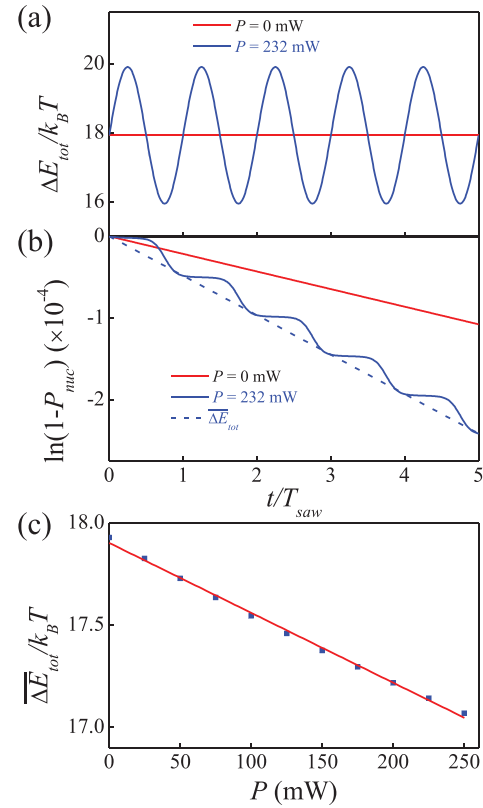


**FIG. 5.** (a) Time dependence of  $\Delta E_{tot}/k_B T$  without and with SAW. (b) Time dependence of  $\ln(1 - P_{nuc})$  without and with SAW. The dashed line represents  $\overline{\Delta E_{tot}}$  with SAW. (c)  $\overline{\Delta E_{tot}}/k_B T$  as a function of  $P$  under SAW. The solid line represents the linear fitting.

nucleation barrier under SAW decreases. Considering a time average, we can obtain the average effective total energy barrier  $\overline{\Delta E_{tot}}$  under SAW, which is shown as the dashed line in Fig. 5(b). Based on the numerical calculation for different  $P$  in Fig. 5(c), we found that  $\overline{\Delta E_{tot}}$  decreases linearly with increasing  $P$ , which is consistent with the experiment results.

In conclusion, we observe a strong reduction of  $J_c$  by the application of SAW in Pt/Co/Ta heterostructures with perpendicular anisotropy. It is found that under SAW, SOT is almost the same, while the DW velocity is greatly enhanced. By fitting the DW velocity with the SAW modified creep law, we demonstrate that the SAW-assisted SOT switching results from the linear lowering of the effective pinning barrier with the SAW power. The results are well explained by the modified droplet model, where the magnetoelastic energy of SAW results in the increase in the average domain nucleation probability. Our finding opens a path for the application of SAW in SOT-based spintronic devices.

This work was supported by the NSFC of China (Grant Nos. 11774139, 11874189, 91963201, 12074025, and 52061135105), the 111 Project under Grant No. B20063, and the Fundamental Research Funds for the Central Universities lzujbky-2021-ct01.

## DATA AVAILABILITY

The data that support the findings of this study are available from the corresponding author upon reasonable request.

## REFERENCES

- <sup>1</sup>X. Qiu, Z. Shi, W. Fan, S. Zhou, and H. Yang, *Adv. Mater.* **30**, 1705699 (2018).
- <sup>2</sup>A. Manchon, J. Železný, I. M. Miron, T. Jungwirth, J. Sinova, A. Thiaville, K. Garello, and P. Gambardella, *Rev. Mod. Phys.* **91**, 035004 (2019).
- <sup>3</sup>I. M. Miron, K. Garello, G. Gaudin, P.-J. Zermatten, M. V. Costache, S. Auffret, S. Bandiera, B. Rodmacq, A. Schuhl, and P. Gambardella, *Nature* **476**, 189 (2011).
- <sup>4</sup>L. Liu, C.-F. Pai, Y. Li, H. W. Tseng, D. C. Ralph, and R. A. Buhrman, *Science* **336**, 555 (2012).
- <sup>5</sup>L. Liu, O. J. Lee, T. J. Gudmundsen, D. C. Ralph, and R. A. Buhrman, *Phys. Rev. Lett.* **109**, 096602 (2012).
- <sup>6</sup>R. Ramaswamy, J. M. Lee, K. Cai, and H. Yang, *Appl. Phys. Rev.* **5**, 031107 (2018).
- <sup>7</sup>W.-G. Yang and H. Schmidt, *Appl. Phys. Rev.* **8**, 021304 (2021).
- <sup>8</sup>C. Thiele, K. Dörr, O. Bilani, J. Rödel, and L. Schultz, *Phys. Rev. B* **75**, 054408 (2007).
- <sup>9</sup>S. Zhang, Y. G. Zhao, P. S. Li, J. J. Yang, S. Rizwan, J. X. Zhang, J. Seidel, T. L. Qu, Y. J. Yang, Z. L. Luo, Q. He, T. Zou, Q. P. Chen, J. W. Wang, L. F. Yang, Y. Sun, Y. Z. Wu, X. Xiao, X. F. Jin, J. Huang, C. Gao, X. F. Han, and R. Ramesh, *Phys. Rev. Lett.* **108**, 137203 (2012).
- <sup>10</sup>L. Thevenard, J.-Y. Duquesne, E. Peronne, H. J. von Bardeleben, H. Jaffres, S. Ruttala, J.-M. George, A. Lemaître, and C. Gourdon, *Phys. Rev. B* **87**, 144402 (2013).
- <sup>11</sup>L. Thevenard, I. S. Camara, S. Majrab, M. Bernard, P. Rovillain, A. Lemaître, C. Gourdon, and J.-Y. Duquesne, *Phys. Rev. B* **93**, 134430 (2016).
- <sup>12</sup>I. S. Camara, J. Y. Duquesne, A. Lemaître, C. Gourdon, and L. Thevenard, *Phys. Rev. Appl.* **11**, 014045 (2019).
- <sup>13</sup>L. Dreher, M. Weiler, M. Pernpeintner, H. Huebl, R. Gross, M. S. Brandt, and S. T. B. Goennenwein, *Phys. Rev. B* **86**, 134415 (2012).
- <sup>14</sup>M. Weiler, H. Huebl, F. S. Goerg, F. D. Czeschka, R. Gross, and S. T. B. Goennenwein, *Phys. Rev. Lett.* **108**, 176601 (2012).
- <sup>15</sup>W. Li, B. Buford, A. Jander, and P. Dhagat, *Physica B* **448**, 151 (2014).
- <sup>16</sup>L. Thevenard, I. S. Camara, J.-Y. Prieur, P. Rovillain, A. Lemaître, C. Gourdon, and J.-Y. Duquesne, *Phys. Rev. B* **93**(R), 140405 (2016).
- <sup>17</sup>W. Edrington, U. Singh, M. A. Dominguez, J. R. Alexander, R. Nepal, and S. Adenwalla, *Appl. Phys. Lett.* **112**, 052402 (2018).
- <sup>18</sup>A. Adhikari and S. Adenwalla, *AIP Adv.* **11**, 015234 (2021).
- <sup>19</sup>M. Matsuo, J. Ieda, K. Harii, E. Saitoh, and S. Maekawa, *Phys. Rev. B* **87**(R), 180402 (2013).
- <sup>20</sup>D. Kobayashi, T. Yoshikawa, M. Matsuo, R. Iguchi, S. Maekawa, E. Saitoh, and Y. Nozaki, *Phys. Rev. Lett.* **119**, 077202 (2017).
- <sup>21</sup>T. Kawada, M. Kawaguchi, T. Funato, H. Kohno, and M. Hayashi, *Sci. Adv.* **7**, eabd9697 (2021).
- <sup>22</sup>R. S. Weis and T. K. Gaylord, *Appl. Phys. A* **37**, 191 (1985).
- <sup>23</sup>J. Yun, Y. Zuo, J. Mao, M. Chang, S. Zhang, J. Liu, and L. Xi, *Appl. Phys. Lett.* **115**, 032404 (2019).
- <sup>24</sup>W. Robbins, *IEEE Trans. Sonics Ultrason.* **24**, 339 (1977).
- <sup>25</sup>D. Sander, *Rep. Prog. Phys.* **62**, 809 (1999).
- <sup>26</sup>G. Woltersdorf and C. H. Back, *Phys. Rev. Lett.* **99**, 227207 (2007).
- <sup>27</sup>H. T. Nembach, P. Martin Pimentel, S. J. Hermsdoerfer, B. Leven, B. Hillebrands, and S. O. Demokritov, *Appl. Phys. Lett.* **90**, 062503 (2007).
- <sup>28</sup>X. Fan, Y. S. Gui, A. Wirthmann, G. Williams, D. Xue, and C.-M. Hu, *Appl. Phys. Lett.* **95**, 062511 (2009).
- <sup>29</sup>C. Huck, H. P. Zidek, T. Ebner, K. C. Wagner, and A. Wixforth, in *IEEE International Ultrasonics Symposium (IUS)*, Prague, 21–25 July (2013).
- <sup>30</sup>J. Kim, J. Sinha, M. Hayashi, M. Yamanouchi, S. Fukami, T. Suzuki, S. Mitani, and H. Ohno, *Nat. Mater.* **12**, 240 (2013).
- <sup>31</sup>S. Chen, D. Li, B. Cui, L. Xi, M. Si, D. Yang, and D. Xue, *J. Phys. D: Appl. Phys.* **51**, 095001 (2018).
- <sup>32</sup>T. Kawada, M. Kawaguchi, and M. Hayashi, *Phys. Rev. B* **99**, 184435 (2019).
- <sup>33</sup>J. Torrejon, F. Garcia-Sanchez, T. Taniguchi, J. Sinha, S. Mitani, J.-V. Kim, and M. Hayashi, *Phys. Rev. B* **91**, 214434 (2015).
- <sup>34</sup>D.-T. Quach, T.-D. Chu, T.-S. Nguyen, T.-T.-P. Doan, X.-T. Nguyen, K.-M. Lee, J.-R. Jeong, N. Kim, H.-J. Shin, and D.-H. Kim, *Curr. Appl. Phys.* **20**, 1026 (2020).
- <sup>35</sup>O. Boulle, S. Rohart, L. D. Buda-Prejbeanu, E. Jué, I. M. Miron, S. Pizzini, J. Vogel, G. Gaudin, and A. Thiaville, *Phys. Rev. Lett.* **111**, 217203 (2013).
- <sup>36</sup>See <https://imagej.net/> for details on reading the Image J software.
- <sup>37</sup>P. Chauve, T. Giamarchi, and P. L. Doussal, *Phys. Rev. B* **62**, 6241 (2000).